Biodata of **Matt R. Kilburn** and **David Wacey**, authors of ***"Elemental and Isotopic Analysis by NanoSIMS: Insights for the Study of Stromatolites and Early Life on Earth"***

Dr. Matt R. Kilburn is manager of the Ion Probe Facility at The University of Western Australia. His lab at UWA is the only lab in the world to house both the Cameca NanoSIMS 50 and the IMS 1280 large-geometry ion probes. He read Planetary Science at University College London, and obtained a Ph.D. on the partitioning of elements during planetary core formation from the University of Bristol. Dr Kilburn became interested in the study of early life while running the NanoSIMS lab at Oxford University, and he now spends an increasing amount of time using SIMS to test the biogenicity of local stromatolites, both ancient and modern.

E-mail: **Matt.Kilburn@uwa.edu.au**

Dr. David Wacey is a biogeochemist at the University of Western Australia. He obtained his D.Phil. from Oxford University studying the effects of SRB on biomineralization. His current research focuses on morphological, chemical and isotopic tracers of primitive Archean life, using cutting edge techniques such as NanoSIMS and Transmission Electron Microscopy. He is the author of a new introductory textbook on Archean life entitled "Early Life on Earth: A Practical Guide", released in 2009.

E-mail: **David.Wacey@uwa.edu.au**

Matt R. Kilburn

David Wacey

V.C. Tewari and J. Seckbach (eds.), *STROMATOLITES: Interaction of Microbes with Sediments*, Cellular Origin, Life in Extreme Habitats and Astrobiology 18, 463–493
DOI 10.1007/978-94-007-0397-1_21, © Springer Science+Business Media B.V. 2011

ELEMENTAL AND ISOTOPIC ANALYSIS BY NANOSIMS: INSIGHTS FOR THE STUDY OF STROMATOLITES AND EARLY LIFE ON EARTH

MATT R. KILBURN[1] AND DAVID WACEY[1,2]
[1]*Centre for Microscopy, Characterisation and Analysis, The University of Western Australia, 35 Stirling Highway, Crawley, WA 6009, Australia*
[2]*School of Earth and Environment, The University of Western Australia, 35 Stirling Highway, Crawley, WA 6009, Australia*

Abstract The ability to unambiguously identify and measure biogenic signals is the key to providing robust evidence for Earth's earliest life. Evidence for life on the early Earth has traditionally been founded on morphological studies, as this is the most obvious and tangible approach. Yet, many morphological features that have been interpreted as biogenic in origin can, in fact, equally be attributed to inorganic processes. Matching chemical signals, for example the presence of carbon and nitrogen, with morphology provides a more robust argument; the ability to correlate in situ isotopic signatures indicative of biological processing with morphological features would provide even more compelling evidence.

Morphological expressions of Earth's earliest life (e.g. microfossils, trace fossils, biominerals or microbial remains within stromatolites) tend to be very small and difficult to analyse in situ. The nano-secondary ion mass spectrometer (NanoSIMS) is a new generation of ion microprobe capable of chemically imaging sub-micron-sized features, providing high-resolution maps of biologically relevant elements such as C, N, P and S. Furthermore, sulphur and carbon isotopic analyses can be performed on micron-sized features with ~1–4‰ precision. This chapter summarises our recent work developing NanoSIMS protocols for isotopic and elemental analyses of candidate biological structures from both modern and ancient rocks.

Keywords Archean • Biogenicity • Biomineral • Carbon • Isotope • Early Life • Microfossil • NanoSIMS • Nitrogen • Pilbara • Stromatolite • Sulphur • Western Australia

1. Introduction

We know that planet Earth is about 4.5 billion years (Ga) old but what is less clear is when it first became home to life. It is unlikely that life gained a foothold before about 3.8 Ga because the first 700 million years of Earth history saw frequent and catastrophic meteorite impacts, which would have repeatedly sterilised the planet.

In contrast, there is abundant evidence for life in rocks younger than 3 Ga. Hence, much work has been carried out over the last ~30 years on the few isolated packets of rocks from the 3.0 to 3.8 Ga time period to study the transition from a non-biological to biological world, and to collect evidence for the first signs of biology that can be used in the search for extraterrestrial life.

Claims for the earliest life on Earth have been numerous (see Wacey, 2009 for a review), but there is still an intense debate about the validity of many of these reports. Ideally, any robust claim for life during this period needs to demonstrate a well-constrained geological context, evidence for biology-like morphology and chemical evidence for metabolic cycling, plus falsification of plausible non-biological origins (Brasier et al., 2006). Unfortunately, this is rarely possible given the great age, minute size and poor preservation of any putative signs of >3 Ga life. Our existing knowledge of >3 Ga life is based largely upon putative microfossils, fractionations of the isotopes of carbon and sulphur and features interpreted as fossilised microbial mats or stromatolites.[1] Each of these, at present, suffers from a degree of uncertainty in their interpretation. Here, we show how geochemical data obtained using nano-secondary ion mass spectrometry (NanoSIMS) can add to our knowledge base.

1.1. ELEMENTAL DISTRIBUTIONS IN STROMATOLITES

It is widely agreed that modern stromatolites are formed by the trapping, binding and cementing of sedimentary grains, as a result of the growth and metabolic activity of micro-organisms (e.g. Walter, 1976). For ancient examples, the formation mechanism is less straightforward because morphologically similar structures can be formed chemically without the aid of biology (e.g. McLoughlin et al., 2008). At present, therefore, stromatolites are a rather controversial indicator of early life on Earth.

The best examples of early Archean stromatolites come from the Pilbara Craton of Western Australia. Here, nodular, wavy-laminated and coniform stromatolites have been described from chert units within the ~3.49 Ga Dresser and ~3.43 Ga Strelley Pool Formations (Lowe, 1980; Walter et al., 1980; Hofmann et al., 1999; Allwood et al., 2006). They have been interpreted as biogenic, based largely upon simple macro-morphological comparisons with rare modern-day

[1] The term "stromatolite" can be used simply as a descriptive term without any indication of biological involvement, defined as "attached, laminated, lithified sedimentary growth structures, accretionary away from a point or limited surface of initiation" (Semikhatov et al., 1979). More commonly, however, the involvement of biology is assumed when a structure is termed a "stromatolite" – "accretionary sedimentary structures, commonly thinly layered, megascopic and calcareous, interpreted to have been produced by the activities of mat-building communities of mucilage-secreting micro-organisms, mainly photoautotrophic prokaryotes" (Schopf, 2006). We adopt the latter terminology in this chapter.

stromatolites, and have been used as a major line of evidence for the emergence of life on the early Earth (see Schopf, 2006 for a review). The problem here is that neither convincing microfossils, mat fabrics, nor elemental patterns indicative of biology have been found in these Archean structures and their biogenicity has been questioned on numerous occasions (Lowe, 1994; Grotzinger and Rothman, 1996; Brasier et al., 2006; McLoughlin et al., 2008). Those who favour a biological mechanism have dismissed the lack of microfossils and biogeochemical signals in such structures as merely due to poor preservation. However, this preservation potential of stromatolites has never been tested in detail, partly due to the lack of suitable technology, and partly due to a lack of coherence between studies of modern microbial mats/stromatolites and fossilised examples from the rock record.

Here, we outline the NanoSIMS methodology for high-resolution elemental imaging of both Phanerozoic and Precambrian stromatolite samples. We present data pertaining to micro- to nano-scale distributions of biologically important elements (e.g. C, N, S) and their spatial relationships within carbonate and silica rock matrices. Characteristic elemental distributions are observed, which may act as a baseline for future studies of Precambrian stromatolites.

1.2. SULPHUR ISOTOPES

Sulphur isotope data ($\delta^{34}S$; where $\delta^{34}S_{V\text{-}CDT}$ (‰) = $[(^{34}S/^{32}S_{sample}) - (^{34}S/^{32}S_{standard})/(^{34}S/^{32}S_{standard})] \times 1{,}000$) from early Archean sedimentary sulphides and sulphates can be informative both about levels of sulphate in the early Archean ocean and about the emergence of sulphate-reducing bacteria (SRB), and possibly, when combined with $\delta^{33}S$ and $\delta^{36}S$ data, the emergence of sulphur-oxidising and disproportionating microbes. Sulphur-processing microbes are often a major component of the modern microbial mat ecosystem (e.g. Baumgartner et al., 2006). Hence, spatially resolved $\delta^{34}S$, $\delta^{33}S$ and $\delta^{36}S$ data may be useful for constraining some of the microbial metabolisms operating in ancient stromatolites.

One problem with sulphur isotope studies has been the limited spatial resolution of conventional isotope measurement techniques. Standard combustion techniques require the isolation of a relatively large amount of sulphide (usually pyrite) from the host rock. Laser ablation inductively coupled plasma mass spectrometry (LA-ICP-MS) allows in situ analysis of sulphur isotopes but still requires sulphides of either ~30 μm or greater in size, or combined analysis of numerous smaller grains. Both of these techniques artificially homogenise the $\delta^{34}S$ signal, and have tended to provide data that is consistent with microbial mediation (Ohmoto et al., 1993; Shen et al., 2001) but also consistent with non-biological formation mechanisms (Runnegar et al., 2001).

A new generation of SIMS instruments (NanoSIMS) has both the spatial resolution and analytical precision to measure individual micro-sulphide grains and help to fill this gap in our knowledge. Here, we outline a methodology for achieving reproducible $\delta^{34}S$ data using NanoSIMS. Although there is still some

work to be done to cross-calibrate this data with more conventional techniques, we demonstrate the ability to measure $\delta^{34}S$ with a precision of 1–4‰ from early Archean pyrites of <5 μm in diameter.

1.3. CARBON ISOTOPES

Carbon isotopes ($\delta^{13}C$) are widely used to argue for the biogenicity of Archean carbonaceous matter. Previous $\delta^{13}C$ data has appeared consistent with biological fractionation (i.e. $\delta^{13}C_{V-PDB} \sim -20$ to -40‰) (e.g. Tice and Lowe, 2004; Walsh and Lowe, 1999). However, technological limitations have meant that most isotopic measurements have not been performed directly on the carbonaceous structures of interest (e.g. an individual microfossil, lining of a trace fossil or carbonaceous lamination). This casts some doubt upon carbon isotope reliability because such bulk rock isotopic measurements introduce the possibility of confusion with other carbon-containing species within the rock or from younger contamination. While standard ion microprobes do allow in situ measurement (e.g. Ueno et al., 2001), they lack the spatial resolution needed to accurately characterise ~1–20 μm-sized objects, sizes typical of putative signs of life in the early Archean. A second problem is that carbon isotopic evidence alone is not necessarily diagnostic for biology because non-biological processes such as "Fischer-Tropsch Type synthesis" can induce $\delta^{13}C$ fractionations of similar magnitudes (McCollum and Seewald, 2006). Therefore, carbon isotope data ideally needs to be accompanied both by an understanding of the geological context of the samples and by high-resolution, in situ mapping of coincident biologically significant elements (e.g. N, S and P) within and around the putative biological structures.

NanoSIMS affords the opportunity to obtain meaningful and reliable $\delta^{13}C$ data from very small objects. This is demonstrated using kerogen found within detrital sandstone grains from the 3.43 Ga Strelley Pool Formation, Western Australia. Isotopic precision of ~3‰ is demonstrated for kerogen linings only 2–5 μm in diameter. For larger carbonaceous objects, >5 μm in diameter, precision of ~1‰ has been achieved (Rasmussen et al., 2008).

2. NanoSIMS Analysis

Secondary ion mass spectrometry uses a high-energy primary ion beam (Cs^+ or O^-) to displace ions from the surface of a sample (secondary ions). These secondary ions are extracted to a mass spectrometer where they are separated by mass and counted. NanoSIMS uses a rastered primary ion beam to produce images much in the same way as a scanning electron microscope (SEM). In this case, however, the images are made up from the sputtered secondary ions, producing chemical maps of the rastered sample surface. NanoSIMS is equipped with a multicollection capability in which a static magnetic field deflects up to five ions

or species into moveable detectors positioned at the appropriate position in the focal plane of the magnet (Hillion et al., 1994). Thus, it is possible to detect and map, for example C, O, N, Si and S simultaneously from the same scanned area. This is particularly important where delicate organic material may be rapidly eroded away by the primary ion beam. The mass spectrometer has been designed to allow high transmission at high mass resolution, that is, to achieve mass resolution that enables the separation of molecular or isotopic interferences on a particular mass (through the use of slits) without drastically reducing the signal. This results in the ability to measure isotope ratios simultaneously from the same sample volume. The precision of isotope measurements depends on the number of counts recorded from the lower abundance isotope. This, together with factors affecting the accuracy of NanoSIMS isotope analyses, will be discussed in more detail below.

2.1. ELEMENTAL MAPPING IN STROMATOLITES

Somewhat fortuitously, the elements commonly representative of organic material, C, N, O, S, have relatively high negative secondary ion yields when sputtered with a Cs^+ primary ion beam. This is due to their high electron affinity. Although N does not readily ionise during SIMS sputtering, it does have a particularly strong emission when coupled to C as the CN^- ion on mass 26. The Cs^+ primary ion beam also has the advantage that it can be focussed to less than 100 nm diameter. This results in the ability to map light elements at high spatial resolution and high sensitivity.

Ions from the transition elements (e.g. Fe, Co, Ni, Cu, Zn) are also commonly associated with/necessary for biological processing, acting as enzyme cofactors and/or potential energy sources for microbial redox reactions (Frausto da Silva and Williams, 2001). In SIMS, these elements yield positively charged secondary ions and are more efficiently produced by sputtering with an O^- primary beam. The O^- beam has a larger diameter than the Cs^+ beam, resulting in a slightly reduced lateral resolution of about 200 nm.

For chemical mapping of the relatively coarse features in stromatolites, secondary ion intensities were more important than high spatial resolution. Aberrations in the spectrometer limit the field of view to a maximum of about 80–100 μm. Therefore, images were typically acquired over a 50–60 μm field of view with an image resolution of 256×256 pixels. In a 50 μm field of view, each pixel measures 195 nm, so for images produced using the Cs^+ primary beam the maximum resolution is defined by the pixel size (as the primary ion beam is smaller than the pixel), but for the images acquired with the O^- primary beam, the maximum resolution is determined by the diameter of the beam.

The secondary ion yields from any given ion species vary depending on the primary ion species, the ionisation potential or electron affinity of the secondary ion, and the nature of the sample matrix. This makes quantification of

multi-component systems extremely difficult with SIMS, and necessitates the use of well-known standards. Ion intensities are not directly comparable with one another, or with themselves in different matrices. This problem is further exacerbated in NanoSIMS where small-scale features of a particular matrix may dominate in only a few pixels of the image, giving rise to ion yield variability at the pixel-to-pixel scale.

As SIMS uses high voltages to accelerate the primary ions, the sample must be conductive. It is therefore necessary to coat non-conducting samples, such as minerals, glasses and ceramics, with a conductive metal film. Typically, a thin (5 nm) gold (Au) coat is used as Au generally does not react with the sample. During sputtering, the Au coat is eroded away exposing the underlying sample surface, which becomes, once again, non-conductive. The ionisation efficiency, and hence the secondary ion yield from the sample, increases with increasing primary ion implantation. As the ion beam erodes the Au coat away, there is an optimum time when the signal is strongest – shortly before the Au coat is entirely removed. After this stage, an electron flood gun may be used to dissipate charge build-up along the edges of the sputter crater, and allow secondary ions to leave the sample surface. This can be problematic when parts of the sample conduct – as the carbon-rich organic layers in stromatolites do.

2.1.1. Stromatolite Samples

Three samples were chosen to demonstrate NanoSIMS elemental mapping capability in stromatolites:

1. A modern lacustrine stromatolite from Lake Thetis, Western Australia (Figs. 1 and 2). Lake Thetis lies approximately 250 km north of Perth, Western Australia and is a permanent saline, alkaline and nutrient poor lake. These conditions exclude most macro-fauna and make the lake ideal for the growth of microbial communities. Grey et al. (1990) described the geomorphology of Lake Thetis. They showed the Lake Thetis basin formed more recently than the Middle Holocene (most likely 3,000–4,500 years B.P.), while radiocarbon dating of lithified stromatolites yielded ages of <1,500 years B.P. A number of terraces are observed surrounding the lake marking abandoned shorelines and recording a relative sea level fall from a high-stand at ~5,000 years B.P. (Brown, 1983). A ~0.5 m fluctuation of lake level between wet and dry periods affects a ~5 m wide strip of the foreshore that undergoes alternating periods of submergence and emergence (Grey et al., 1990).

   Five types of living microbial mats have been identified from Lake Thetis (crenulated, nodular, filamentous, diatomaceous and flocculent), each dominating different, roughly concentric zones in the lake and its surrounds (for details see Grey et al., 1990). Lithified stromatolite platforms and domes (Fig. 1a) occur on three terraces around the lake margin. Stromatolite domes are composed mostly of aragonite, are typically 50–100 cm in diameter and occur on the lowest terrace, defining the lake margin. Crenulate and nodular

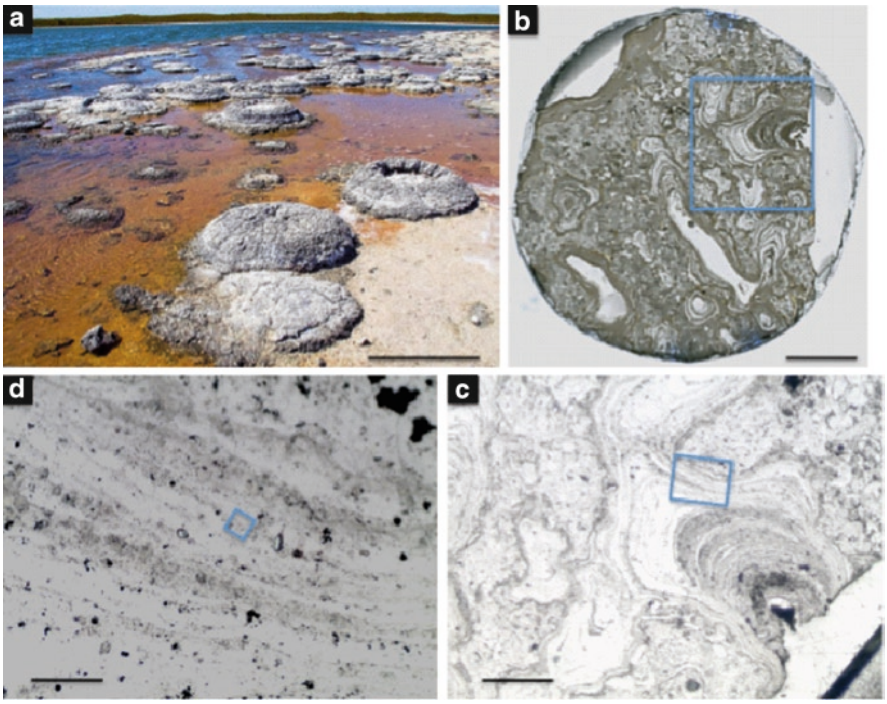

Figure 1. Modern lacustrine stromatolites from Lake Thetis, Western Australia. (**a**) Field photograph of <1,500-year-old lithified stromatolite domes associated with living nodular and diatomaceous microbial mats and pink microbial sediment, Lake Thetis shoreline; (**b**) scanned thin section of the outer part of a lithified stromatolite dome from Lake Thetis shoreline. The thin section has been cut into a 10 mm diameter circle for insertion into the NanoSIMS and a sub-area containing a micro-stromatolite has been selected for study (boxed area enlarged in **c**); (**c** and **d**) photomicrographs at increasing magnification of boxed area in (**b**) showing how individual laminae or groups of laminae can be targeted by NanoSIMS. Scale bar is 1 m for (**a**), 2 mm for (**b**), 600 μm for (**c**), 80 μm for (**d**).

living mats are intimately associated with these lithified domes but it is not clear whether they are now actively contributing to the domal stromatolite growth. In cross-section, the domes show variable textures, ranging from clotted (thrombolytic) in the dome centres to crudely laminated to distinctly laminated and rare branching columns at the outer margins. Lake Thetis stromatolites are interpreted to have formed by biologically induced carbonate precipitation (Grey et al., 1990).

The branching columns observed in some Lake Thetis stromatolites are of particular relevance to studies of ancient life. Branching is common in Precambrian stromatolites but is rarely observed in Phanerozoic examples. This is thought to be a consequence of increased bioturbation and grazing in the Phanerozoic inhibiting the development of mucilaginous layers that protect

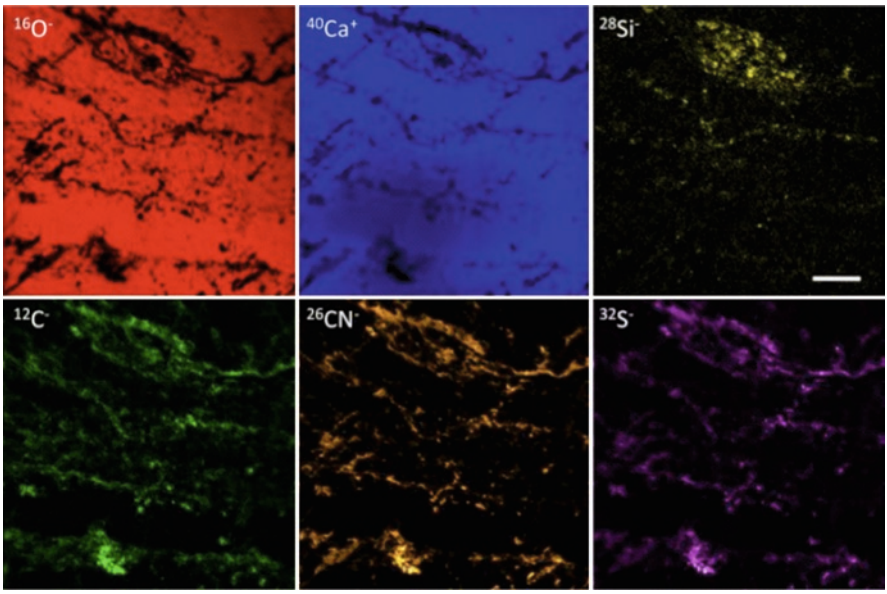

Figure 2. NanoSIMS ion images of laminations within a Lake Thetis stromatolite. The laminae run from left to right across the field of view and are highlighted by bright areas in the $^{12}C^-$, $^{26}CN^-$ and $^{32}S^-$ images, and black areas in the $^{16}O^-$ and $^{40}Ca^+$ images. The carbon image has been corrected for background carbon from calcium carbonate. $^{12}C^-$, $^{26}CN^-$ and $^{32}S^-$ correlate with one another spatially and in terms of signal intensity. $^{16}O^-$ and $^{40}Ca^+$ correlate with one another but anti-correlate with $^{12}C^-$, $^{26}CN^-$ and $^{32}S^-$, confirming that the observed $^{12}C^-$, $^{26}CN^-$ and $^{32}S^-$ signals come from organic material not from any carbonate or sulphate mineral phases. $^{28}Si^-$ shows some correlation with $^{12}C^-$, $^{26}CN^-$ and $^{32}S^-$, this is discussed in the text. Increased colour intensity reflects increased relative abundance of each ion. The *darker blue* colour in the lower half of the $^{40}Ca^+$ image is due to a decrease in ion signal when the conductive gold coat was sputtered away; scale bar is 8 μm.

the growing stromatolite. The Lake Thetis stromatolites therefore give a rare opportunity to study a potential true modern analogue for the most ancient stromatolites at the micro- to nano-scale. Our sample for NanoSIMS study comes from the outer margin of a domal stromatolite that exhibits laminations and micro-stromatolitic texture (Fig. 1b–d).

2. A modern marine stromatolite from Shark Bay, Western Australia (Fig. 3). Shark Bay, approximately 700 km north of Perth is home to diverse and abundant stromatolites and microbial mats. These occur in the intertidal and subtidal zones of a hypersaline embayment (Hamelin Pool), along almost 100 km of shoreline (Playford, 1990). Nine types of microbial mats have been identified in the bay, based on their surface morphology (Logan et al., 1974; Playford, 1990), along with domal and columnar stromatolites <4,000 years old. Some stromatolites are still actively growing today and a vertical accretion rate of ~0.4 mm/year is suggested by radiocarbon dating (Reid et al., 2003). Most Hamelin Pool stromatolites are unlaminated or weakly laminated with irregular

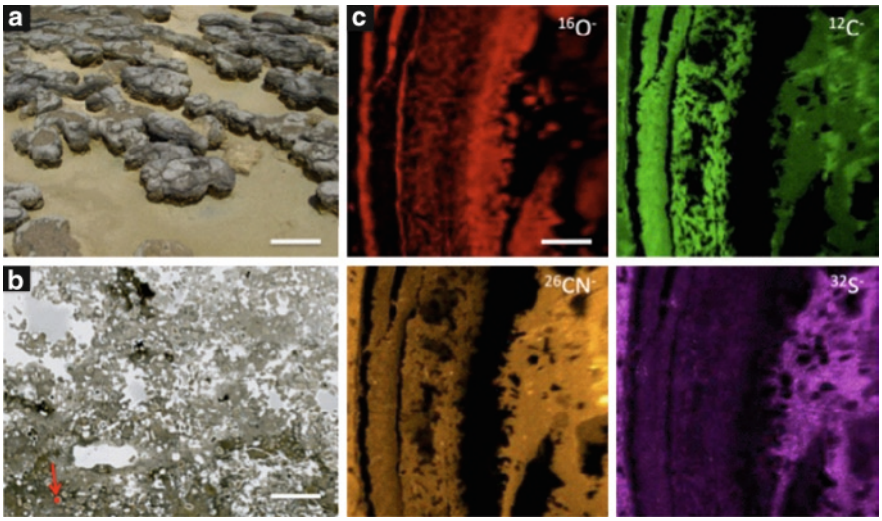

Figure 3. Modern marine stromatolites from Shark Bay, Western Australia. (**a**) Field photograph of living stromatolites from Hamelin Pool, Shark Bay; (**b**) scanned thin section of part of a lithified stromatolite collected from the shoreline of Hamelin Pool. This exhibits a rather clotted texture, similar to the "unlaminated calcarenite" described by Reid et al. (2003); (**c**) NanoSIMS ion images of oxygen, carbon, nitrogen (measured as CN^-) and sulphur from the area arrowed in (**b**). Increased colour intensity reflects increased relative abundance of each ion. The carbon image has been corrected for the background contribution from $CaCO_3$. $^{12}C^-$, $^{26}CN^-$ and ^{32}S correlate with one another but anti-correlate with $^{16}O^-$ just as they do in the Lake Thetis example. Scale bar is 50 cm for (**a**), 2.5 mm for (**b**), 10 μm for (**c**).

fenestral networks, quantities of trapped sediment and irregular outer surfaces, and are thought to be constructed mostly by pustular and colloform mat communities. More rarely, smooth mat communities construct well-laminated columns and mounds in the intertidal to shallowest subtidal zone (Playford, 1990). A number of recent studies have documented the microbial makeup of the stromatolites (e.g. Burns et al., 2004; Papineau et al., 2005) and some of the nine types of microbial mats (Allen et al., 2009) to begin to decipher the role of individual microbial groups in stromatolite construction at Shark Bay.

Our sample for NanoSIMS comes from the mid-intertidal zone. The fabric approximates that of the "unlaminated calcarenite" described by Reid et al. (2003) (compare our Fig. 3b with Reid et al., 2003, Plate 49, 1b and 1c), consisting of a mottled network of limestone (micrite, carbonate sand, peloids and oolites) and fenestrae (seen as holes in thin section). Occasional bivalve fragments and foraminifera are also cemented by micrite. This type of stromatolite was interpreted by Reid et al. (2003) as being formed by pustular microbial mats whose irregular surface morphology has inhibited laminae development. Our NanoSIMS data shows some of the chemical signals that are retained during the transformation from a living microbial mat to a stromatolite that can be preserved in the rock record.

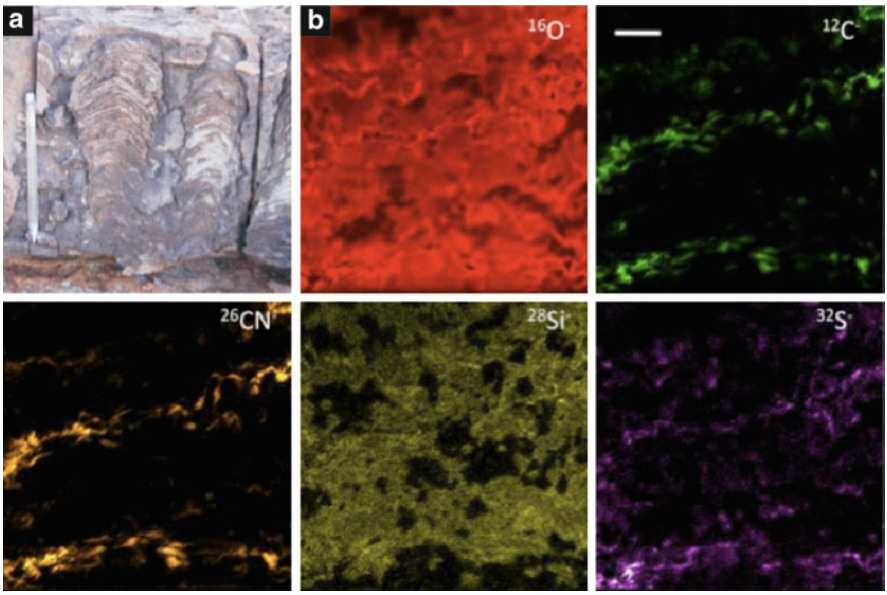

Figure 4. Ancient stromatolites from the ~2.72 Ga Tumbiana Formation, Western Australia. (**a**) Field photograph of columnar stromatolites from the Meentheena carbonate Member of the Tumbiana Formation (courtesy of the Geological Survey of Western Australia); (**b**), NanoSIMS ion images of oxygen, carbon, nitrogen (measured as CN^-), silicon and sulphur from a 60×60 μm^2 area of a Tumbiana stromatolite. Similar elemental distributions to the modern examples are observed, with laminations defined by spatial correlation and intensity of carbon, nitrogen and sulphur (partly). Increased colour intensity reflects increased relative abundance of each ion. Scale: pen in (**a**) is 12 cm long; scale bar in (**b**) is 10 μm.

3. An ancient stromatolite from the 2.72 Ga Tumbiana Formation of Western Australia (Fig. 4). Diverse stromatolites (domical, columnar, branching and stratiform) are found in the Meentheena Carbonate Member of the Tumbiana Formation, part of the Fortescue Group, Pilbara, Western Australia (Walter, 1972). The dominant microstructure consists of groups of laminations organised as bulbs, varying in size from several hundred microns to several centimetres in height (Lepot et al., 2008). Micritic calcium carbonate layers alternate with thinner siliceous layers. These stromatolites formed mainly by in situ precipitation (Grotzinger and Knoll, 1999) in either shallow seawater (e.g. Sakurai et al., 2005) or a large lake (Buick, 1992).

   Recent work has demonstrated clusters of "cell-like" carbonaceous globules associated with nano-aragonite crystals in bulbous Tumbiana stromatolites (Lepot et al., 2008); these carbonaceous globules contain many of the same functional groups as modern bacteria. This, taken together with the morphological complexity and close comparison to modern stromatolites of the

Tumbiana examples, provides strong evidence for their biogenicity. Hence, this sample was chosen for NanoSIMS study as an example of one of the oldest widely accepted biogenic stromatolites.

2.1.2. Stromatolite Results

2.1.2.1. Lake Thetis Stromatolite

Several ~ 50×50 μm^2 laminated areas of the Lake Thetis stromatolite were mapped using both the Cs^+ and O^- primary ion beams. Similar chemical patterns were observed in each area and representative images are shown in Fig. 2. The most important result is the close correlation of the carbon, nitrogen and sulphur images. These images highlight chemically the laminations running from left to right across the field of view (Fig. 2). The near identical spatial distribution of these three elements, together with changes in intensity that parallel one another (i.e. a very bright area on the carbon map correlates with very bright areas on the nitrogen and sulphur maps), appears to be a characteristic of microbial material preserved as wavy laminations within the carbonate matrix. Under the optical microscope (e.g. Fig. 1d), it is difficult to distinguish the morphology of an individual lamina. However, the high spatial resolution of the NanoSIMS allows us to see in greater detail; we see that laminae commonly comprise a mixture of networks of anastomosing microbial material and some larger clumps or grains of microbial material. In addition, we can clearly observe small deviations and undulations in laminae and one area, in particular, where microbial material appears to join adjacent laminae (just north-east of the centre of Fig. 2). This could, for example, represent filamentous microbes that were growing up through trapped sediment towards the mat surface.

It is important to confirm that the elemental distributions of C, N and S are due to organics/microbial matter and not other mineral phases. This can be done by comparing the C, N and S maps with those for oxygen, which will highlight carbonate and sulphate minerals, and with images of the cations contained in known matrix minerals (in this case, calcium from calcium carbonate). The O and Ca images correlate well with one another but anti-correlate with C, N and S indicating that the C, N and S distributions are indeed due to preserved microbial material in this stromatolite. In ancient stromatolites, silicon will be a useful element to analyse as many ancient stromatolites are partially or entirely silicified. In this case, Si is merely an accessory phase, but it does show some correlation with C, N and S. This may be due to the trapping of windblown silica rich particles by the microbes or may be due to precipitation catalysed by the metabolic activity of the microbes. Further investigation is needed to distinguish these processes.

It is worth noting that NanoSIMS images give only the relative concentrations of each of the elements; it is not possible to obtain an absolute concentration. Additionally, it is very difficult to obtain meaningful ratios of elements present in a sample. For example, one may be interested in the N/C ratio of the microbial material to provide information about the parts of microbes that are preserved in stromatolites. The apparent N/C ratio of a sample in SIMS is controlled not only

by its true N/C ratio but also by SIMS instrumental parameters that control CN^- and C^- ion yields, and by the matrix that the N- and C-rich material lies in. Such ratios were not attempted in this study.

2.1.2.2. Shark Bay Stromatolite

Several ~ 50×50 μm^2 areas of the Shark Bay stromatolite were mapped using both the Cs^+ and O^- primary ion beams. Since this stromatolite was not laminated when viewed under the optical microscope (Fig. 3b), we decided to target the peloidal to oolitic trapped grains to investigate the distribution of microbial material in these areas. Representative NanoSIMS ion images from the coatings of these grains are shown in Fig. 3c. A similar elemental distribution is observed to that seen in the Lake Thetis stromatolite. Carbon, nitrogen and sulphur distributions are closely correlated spatially, and oxygen shows almost exact anti-correlation. Again, this appears characteristic of microbial material interspersed with precipitated carbonate cement. In this case, some of the laminae are almost entirely organic, some are almost entirely carbonate cement and some (e.g. just left of centre in Fig. 3c) appear to be a mixture of microbial material and carbonate. The sulphur distribution does not correlate exactly with carbon and nitrogen. This may be due to the presence of some sulphate minerals or an as-yet-unidentified sulphur phase.

2.1.2.3. 2.72 Ga Stromatolite

The ~2.72 Ga Tumbiana Formation stromatolite was investigated in an identical manner to the modern examples from Shark Bay and Lake Thetis. Representative NanoSIMS ion images are shown in Fig. 4b. Despite the great age of this stromatolite, similar elemental distributions are observed to those found in the modern examples. Once again carbon and nitrogen correlate spatially with one another and highlight laminations running from left to right across the field of view (Fig. 4b). Sulphur correlates, in part, with carbon and nitrogen, but the correlation is not as well matched as in the modern examples. Again, we see that the laminations are not simple; they consist of intertwined strands and anastomosing networks of organic material. The silicon image shows that the original carbonate structure has been partly silicified and this appears to have masked much of the (anti)correlation of C, N and S with oxygen. Although the elemental patterns observed here are very similar to those in the modern examples, for stromatolites of this great age we must test that the signals we see are truly ancient and biological. Nitrogen is a key biological element that is concentrated by cellular products, along with carbon, via biotic fixation processes (e.g. Frausto Da Silva and Williams, 2001). Although the mere presence of nitrogen cannot be used to infer biogenicity, a close correlation on a sub-micron scale of nitrogen with carbon has been used as an indicator of biological processing in well-preserved carbonaceous microfossils from both the ~1,900 Ma Gunflint Chert of Canada (Robert et al., 2005) and the ~850 Ma Bitter Springs Chert of central Australia (Oehler et al., 2006), where the carbon and nitrogen chemical maps show direct correlation with optical images

of the microfossils. In contrast, an abiogenic source of nitrogen in organic matter requires specific conditions and reactants. Nitrogen has been incorporated into organic matter abiogenically by high temperature Fischer Tropsch synthesis, using CO, H_2, NH_3 and a metal catalyst, in laboratory experiments attempting to replicate the formation of organic matter in meteorites (Kung et al., 1979; Hayatsu et al., 1972). However, field observations of the Meentheena Carbonate Member, indicating deposition in a lacustrine or shallow marine environment with little hydrothermal influence (e.g. Lepot et al., 2008), are inconsistent with conditions required for such abiogenic nitrogen synthesis. Sulphur is likewise concentrated by biotic fixation processes (Frausto Da Silva and Williams, 2001) and while its mere presence may be due to both biological and abiological concentration, a positive correlation with carbon and nitrogen lends further support to a biological formation mechanism.

The syngeneity of the Tumbiana chemical signals is unquestionable since the laminations with which they directly correlate have been shown to be primary (bio)sedimentary structures (e.g. Buick, 1992). NanoSIMS analysis of the Tumbiana stromatolites adds further support to a biological origin for these structures (cf. Lepot et al., 2008) and provides chemical signals that may act as a baseline for the study of other Precambrian stromatolites of unknown biogenicity.

2.2. SULPHUR ISOTOPE ANALYSIS

Here, we describe a method we have developed for measuring S isotope ratios in micron-sized grains using the high-resolution imaging capability of the NanoSIMS.

2.2.1. NanoSIMS Setup

All sulphur isotopic measurements were obtained using a Cs^+ primary ion beam focused to about 100 nm. The secondary ions $^{12}C^-$, $^{12}C^{14}N^-$, $^{32}S^-$ and $^{34}S^-$ were recorded simultaneously. The smallest pyrite grains (Type 1, see below) typically measure 2–3 μm in size, which are too small to be analysed by a static beam individually with sufficient stability and precision. It was therefore necessary to raster the primary ion beam over an area of 12×12 or 15×15 μm, producing an image from which the isotope data could be extracted. The images were obtained at a resolution of 256×256 pixels, each pixel measuring 47–59 nm, with a count time of 5 ms per pixel. Each pixel records the counts for each secondary ion, corrected for dead time (44 ns) and detector yield. Cameca NanoSIMS Image processing software was used to ratio the $^{34}S^-$ counts to the $^{32}S^-$ counts for the pixels defining each individual grain in an image. Variations in the S isotope ratio at the pixel-to-pixel scale are overshadowed by the large counting error on each pixel. It was therefore necessary to use the mean ratio value for the group of pixels defining a particular grain in the ion images. Charge compensation with the electron gun

was not necessary as the pyrites maintained electrical conductivity throughout the analysis.

2.2.2. Factors Affecting Accuracy and Precision

2.2.2.1. Detector Ageing

The high electron affinity of S means that the negative secondary ion yield is very high under Cs^+ bombardment. On the one hand, this is good for generating enough counts to get good counting statistics, but has the disadvantage of generating so many counts that detector ageing and quasi-simultaneous arrivals (QSAs) at the electron multiplier (EM) become important issues (Slodzian et al., 2001). Detector ageing occurs when the secondary ion signal is so intense that the first dynode of the EM begins to degrade. The detector response changes over the course of its lifetime, but with intense signals (more than 400,000 counts per second) the effect is much more rapid. In analyses using two EMs where one EM has a very intense signal, the change in response of the detector with the high intensity signal can artificially influence the measured isotope ratio. To avoid this, the secondary ion flux can be kept low by cutting the beam with slits and apertures, which also increases the mass resolution to give better peak shapes. If necessary, a correction can be applied to the isotope ratio by monitoring the detector response during the analysis. Faraday cup (FC) detectors, which do not suffer from ageing effects or QSA, could not be used for this type of analysis because the response time of the FC is too slow and the background noise is too great to produce the good quality images needed for isotope ratio measurements.

2.2.2.2. QSA Effects

QSA presents a far more difficult artefact to overcome. This occurs when the ionisation efficiency is so high that a single primary ion may sputter two or more secondary ions, which travel through the mass spectrometer together and hit the first dynode of the EM more or less simultaneously. As EMs count the pulses generated by the incoming ions, simultaneous arrivals are measured as single pulses. This will, of course, have an effect on the isotope ratio, as part of the signal will not be detected. While QSA is not dependent on count rate, the magnitude of the effect is. High count rates at the detector can lead to contributions of up to 100‰ (10%) from QSA alone. This phenomenon is particularly problematic when measuring natural abundance isotopes with NanoSIMS. A theoretical correction model exists for a measured ratio (R): $R_{meas} = R_{true} \times (1 + \beta \times K)$, where K is the ratio of secondary to primary ion current and $\beta = 0.5$ (Slodzian et al., 2004; Hillion et al., 2008). However, experiments have shown that this value of β deviates significantly from 0.5, with observed values between 0.5 and 1 (e.g. $\beta = 0.69$ in Slodzian et al., 2004). In our preliminary analyses, neither the theoretical value of $\beta = 0.5$ nor the experimental value of $\beta = 0.69$ was found to adequately correct for QSA effects observed at our analytical conditions in the NanoSIMS 50.

Our modified experimental approach uses an empirical correction derived from measuring the change in isotope ratio at different primary to secondary

ion current ratios. This is achieved by measuring the $^{34}S/^{32}S$ isotope ratio with a constant primary ion current, while varying the secondary ion current with slits and/or energy offsets. Plotting the $^{34}S/^{32}S$ ratio against K for a particular sulphide grain produces a linear relationship. The slope of the linear regression may then be used as the correction coefficient, β, in the data processing (cf. Slodzian et al., 2004; Hillion et al., 2008). This approach was used on each grain measured, producing an individual, empirically derived correction factor for each measurement. Another critical aspect of the QSA correction is that the relationship between the isotope ratio and the primary/secondary ion current only becomes linear after the secondary ion yield has reached a steady state.

For pyrite, this requires a primary ion implantation dose of $\sim 8 \times 10^{16}$ cm^{-2}. Under these analysis conditions, this requires approximately 150 min (1.4 pA primary beam current, 12×12 μm raster size). Figure 5 explains the correction of our raw data for QSA effects and presents the uncertainty associated with this correction.

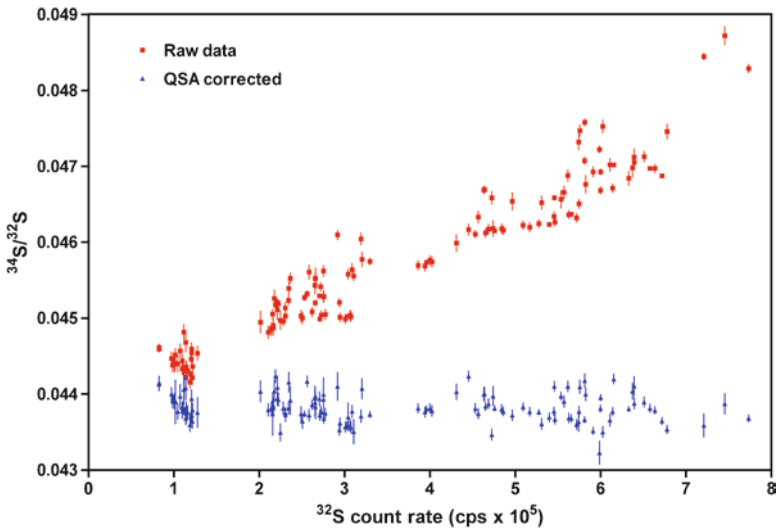

Figure 5. A comparison of raw NanoSIMS $^{34}S/^{32}S$ data and QSA corrected $^{34}S/^{32}S$ data. The raw data shows a strong positive correlation with ^{32}S count rate and a large spread of $^{34}S/^{32}S$ ratios; this correlation is merely an instrumental artefact due to QSA. The raw data is corrected by applying a series of linear regressions through data from each sulphide grain (i.e. one regression line through data for the CP1 standard, one through data for Type 2 pyrite, one through data for Type 3 pyrite, and one through data from each individual Type 1 pyrite grain). The errors associated with the QSA correction are dependent on the quality of fit of each regression line. These errors are propagated (added to the Poisson counting errors) to obtain the error bars shown on the QSA corrected data. The uncertainties associated with the QSA correction are generally only slightly larger than the Poisson counting errors. Hence, the spread in $^{34}S/^{32}S$ for QSA corrected data can be considered real. The sample data is then calibrated to V-CDT using the data obtained from the CP1 standard, which has a known $^{34}S/^{32}S$ ratio, a known V-CDT value and known analytical errors (-4.6 ± 0.2‰).

2.2.2.3. Poisson Counting Precision

As mentioned above, EMs are ion-counting detectors, which means their precision is dependent on Poisson counting statistics. The internal precision of a measurement derived from two EM detectors is given by:

$$\text{Precision (\%)} = \sqrt{(1/N_1 + 1/N_2)} \times 100$$

where N_1 and N_2 are the total counts on ion species 1 (^{32}S) and 2 (^{34}S), respectively. As ^{32}S represents 95.0% of the total S abundance (versus only 4.2% for ^{34}S), the counts from ^{32}S are over 20 times higher than ^{34}S. This makes the ^{32}S contribution to the counting precision largely negligible. Therefore, the precision can be approximated as $1/\sqrt{N_2}$, the counts on the lower abundance isotope. To achieve an isotope ratio measurement with an internal precision of 1‰ (0.1 %), one million counts from the lower abundance isotope are needed. For our analyses, multiple images were acquired sequentially, which were then added together to improve the counting statistics. For the standard (CP1) and Type 2 and 3 pyrites, where the grain filled the entire image frame, five images were acquired with a total acquisition time of 13 min. For the Type 1 pyrites, fifteen images were acquired, with a total time of 35 min per measurement, resulting in several million counts for ^{34}S over a typical 12 × 12 μm image. A typical 2–3 μm-sized grain, from the same raster size and under the same analytical conditions, would yield between 100,000 and 500,000 counts on ^{34}S, giving precisions of between ~3 and 1.5‰, respectively.

2.2.2.4. Reproducibility

Poisson counting statistics only represent the theoretical "best" precision possible. More critical for the NanoSIMS analyses is the reproducibility, or external precision, of the isotope measurements. This can be difficult to ascertain when there is inherent variability between grains in the sample. For the micron-sized pyrites (Type 1), it is necessary to confirm that any apparent natural grain-to-grain variation in the isotope ratio was not simply due to poor reproducibility in the measurements.

As we were unable to measure the reproducibility by measuring multiple Type 1 grains to determine the standard deviation, we demonstrated that the uncertainty due to the Poisson counting statistics is a close approximation of the external precision. To illustrate this, we acquired images of the CP1 standard and large grains (Type 2) in the sample where the grains were big enough to fill the entire imaged area. Using image processing software, we measured the isotope ratio for small sub-regions (discrete groups of pixels) to create areas similar in size to the smaller Type 1 pyrite grains, and compared the isotope ratios from the different areas (Fig. 6). The ratios calculated for each individual area (Fig. 6b–e) had essentially the same value as the ratio for the whole image (Fig. 6a), producing a small standard deviation between areas. The internal precision for the whole area, propagating Poisson counting error, uncertainty on the QSA correction, and conversion to per mil was 1.2‰, while the internal precision of the sub-regions was

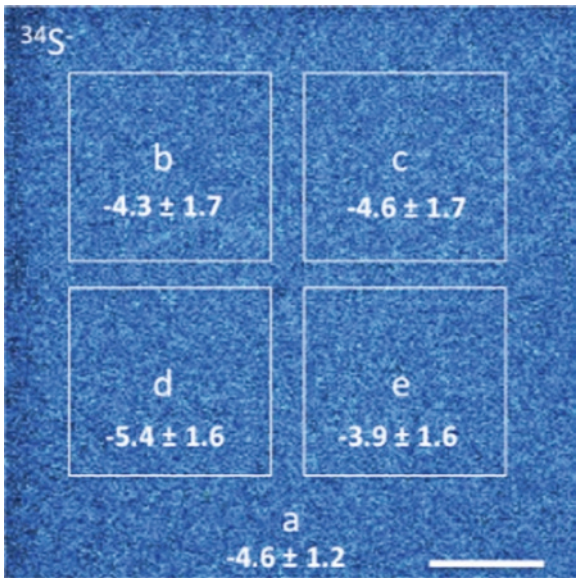

Figure 6. NanoSIMS ion image of $^{34}S^-$ from the CP1 standard, with $\delta^{34}S_{V\text{-}CDT}$ (‰) values superimposed to illustrate data reproducibility within a single analysis. 10–12 μm analysis areas (a) were split into sub-areas (b–e) of approximately equal size to Type 1 pyrites. The standard deviation (reproducibility) between these sub-areas is 0.6‰, which is smaller than the average Poisson error due to counting statistics (1.2–1.7‰). This gives $\chi^2 < 1$ and indicates that the reproducibility was good and the analyses are of sufficient quality. See text for further details. Scale bar is 2 μm.

1.6–1.7‰ due to the smaller number of pixels, and thus a lower number of counts, in the sub-regions. The standard deviation of the sub-regions (the reproducibility) was 0.6‰. As the Poisson counting error is the theoretical limit of counting precision, the 'true' uncertainty of the measurements here is given by the propagated counting statistics, i.e. the larger of the two errors. The quality of the analysis can then be expressed using the χ^2 relationship:

$$\chi^2 = (\text{error mean} / \text{Poisson})^2$$

A "good" measurement will have a reproducibility that is equal to or better than the counting statistics, giving a χ^2 of 1 or less. All measurements on the standard satisfied this test. Hence, if variations in $\delta^{34}S$ that are larger than the Poisson error are seen on a grain-to-grain scale amongst the Type 1 pyrites, they can be considered a real, natural variation in S-isotope fractionation.

2.2.2.5. Accuracy

The accuracy of an isotopic measurement is a function of the mass fractionation imparted by the instrument (instrumental mass fractionation or IMF), which incorporates effects due to the sputtering, ionisation, extraction, transmission and detection of the secondary ions (Winterholler et al., 2008). IMF effects associated with the sputtering and ionisation of the sample include matrix effects and sample preparation factors such as topography. IMF effects due to the extraction and transmission of secondary ions generally remain constant throughout an analytical session. The IMF effects associated with the detection and measurement of secondary ions relate to issues of QSA and dead time, which have already been

addressed. For our flat, polished samples topography is not significant, and as the standard is mounted alongside the sample, effects due to movement on the sample holder are minimal.

To determine IMF, we calibrated our CP1 standard and Strelley Pool sample using LA-ICP-MS. After correcting for dead time and QSA effects, we used the standard calibration formula:

$$\delta^{34}S_{IMF} = \left[\left[\left(^{34}S/^{32}S\right)_{CP1\text{ - }NanoSIMS} / \left(^{34}S/^{32}S\right)_{CP1\text{ - }LA\text{ - }ICP\text{ - }MS}\right] - 1\right] \times 1{,}000$$

to obtain a NanoSIMS IMF of −23‰ relative to the known absolute $^{34}S/^{32}S$ ratio of CP1. This is of a similar magnitude to the −20‰ IMF reported by Graham and Valley (1992) using a Cameca IMS 4f instrument.

With regard to matrix effects, Riciputi et al. (1998) investigated the matrix effects associated with different sulphide chemical compositions in SIMS. Their data showed a maximum of ~3‰ fractionation between seven different sulphide minerals when using the Cs^+ primary ion beam. Specifically, the fractionation between pyrite (FeS_2; our sample) and chalcopyrite ($CuFeS_2$; our standard) was <1‰ (Riciputi et al., 1998, Table 5 and Fig. 6). We confirmed that there is only a small matrix effect between pyrite and chalcopyrite by measuring several Type 3 pyrites using the same LA-ICP-MS instrumentation as for CP1 (Wacey et al., 2009). After the 23‰ IMF correction, there was an added discrepancy of ~2‰ between the average Type 3 $\delta^{34}S$ measured by LA-ICP-MS and that measured by NanoSIMS. This discrepancy may be due to some small matrix effect (1–2‰) but it is also of the same magnitude as the analytical error associated with the NanoSIMS measurements. Hence, we conclude that in our experiment the change in matrix between pyrite and chalcopyrite does not significantly affect IMF.

All $^{34}S/^{32}S$ ratios were converted to $\delta^{34}S$, in ‰, using the following formula:

$$\delta^{34}S(\%) = \left[\left(^{34}S/^{32}S\text{sample}\right) - \left(^{34}S/^{32}S\text{standard}\right)/\left(^{34}S/^{32}S\text{standard}\right)\right] \times 1{,}000$$

and all $\delta^{34}S$ values were normalised to the CP1 standard of $\delta^{34}S_{V\text{-}CDT} = -4.6$‰. Errors associated with the known LA-ICP-MS value for CP1 (±0.2‰) were propagated to obtain a final ‰ value for each sample grain. Isotope measurements of Strelley Pool sample pyrite grains were bracketed between CP1 standard measurements.

2.2.3. Samples

The samples used for developing a NanoSIMS sulphur isotope methodology come from a silicified sandstone at the base of the ~3.43 billion-year-old Strelley Pool Formation from the Pilbara of Western Australia (Wacey et al., 2006). The Strelley Pool Formation is a regionally extensive marker horizon that separates the thick, dominantly volcanic successions of the 3.525–3.427 Ga Warrawoona and 3.35–3.315 Ga Kelly Groups (Hickman, 2008). It is internationally acknowledged as one of the world's most important early Archean formations for the

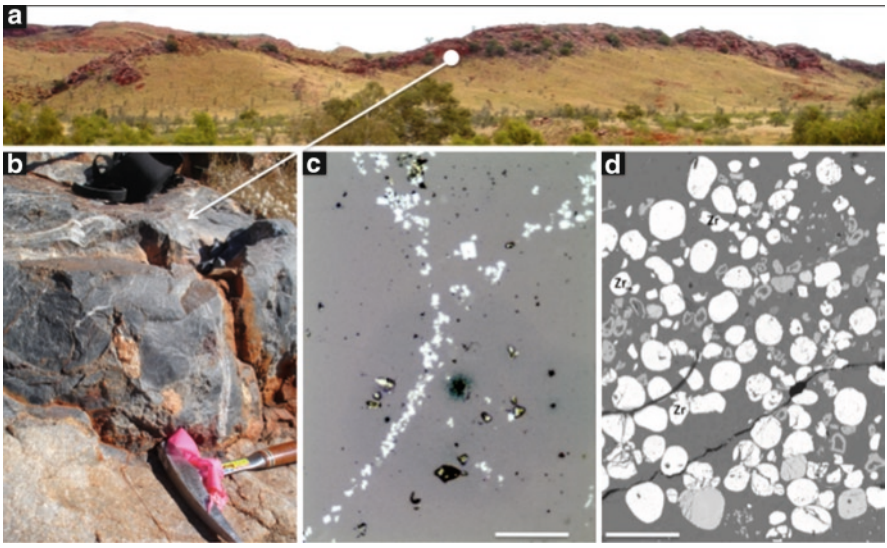

Figure 7. Pyrite samples for sulphur isotope analysis. (**a**) Field photograph looking south showing a ridge of the ~3.43 Ga Strelley Pool Formation, approximately 5 km east of Strelley Pool, Western Australia. The Formation dips almost vertically away from the viewer (to the south); (**b**) outcrop photograph of well-preserved grey-black sandstone, containing Type 1 and 2 pyrites, from the base of the Strelley Pool Formation; (**c**) reflected light photomicrograph of Type 1 pyrite (*white*) coating large, rounded detrital quartz grains (*grey*). A cube of Type 2 pyrite can be seen just above the centre of this image; (**d**) Reflected light photomicrograph of Type 3 detrital pyrite grains (*white*) occurring in a placer-type deposit with chromite (*light grey*), rutile (*light grey rings*) and zircon (Zr). Scale bar is 50 μm for (**c**) and 500 μm for (**d**).

study of early life on Earth. The sandstone unit exhibits low angle cross-bedding, channel bedforms and relatively high textural and compositional sediment maturity, consistent with deposition in a high energy regime (Wacey et al., 2006, 2010a). At the sample locality (Fig. 7a, b), near to Strelley Pool, the sandstone lies unconformably on eroded 3.515 Ga Coonterunah Subgroup volcanics, providing one of the earliest preserved land surfaces in the rock record (Lowe, 1983; Buick et al., 1995). The basal sandstone was lithified by the time that the overlying laminated carbonates (including putative stromatolites) of the Strelley Pool Chert were deposited. Early silicification is clearly indicated by the presence of rounded, intraformational clasts of the sandstone within higher beds of the sandstone itself as well as within the overlying chert. This is an important observation that helps to constrain the age of the pyrite within the sandstone. Four types of pyrite can be identified within the Strelley Pool sandstone. Type 1 pyrites are micron-sized grains coating many of the detrital framework sandstone grains (Fig. 7c). These are found in areas where the sandstone is black and evidently very well preserved, and also in black intraformational clasts higher up in the sandstone member.

They are thus interpreted as approximately syn-depositional (~3.43 Ga) in age. Type 2 pyrites are larger, cubic pyrite crystals (Fig. 7c, square just above centre). These likely formed by the dissolution and re-crystallisation of Type 1 pyrites during low-grade metamorphism sometime prior to the last significant metamorphic event in this area at ~2.9 Ga. Type 3 pyrites are well rounded and partially eroded detrital pyrite (older than 3.43 Ga) occurring in spatially restricted placer deposits with other heavy minerals such as zircon, chromite and rutile (Fig. 7d). Type 4 pyrite consists of small cubic or rhombic crystals sealed within detrital siliceous grains. These are rather rare and were not analysed for $\delta^{34}S$ in this study, although they occur in close proximity to areas analysed for $\delta^{13}C$ (see Sect. 2.3 below).

2.2.4. Sulphur Isotope Results

Type 1 pyrite: Sixty-nine Type 1 pyrite measurements, from four separate analysis areas of the thin section, have a range of $\delta^{34}S_{V\text{-}CDT}$ from −11.7‰ to 6.3‰. The mean value for these grains is −2.1‰.

Type 2 pyrite: Forty-four measurements from Type 2 pyrites have a range of $\delta^{34}S_{V\text{-}CDT}$ from −6‰ to 3.4‰. The mean value for these grains is −2.9‰.

Type 3 pyrite: Eight measurements from Type 3 pyrites have a range of $\delta^{34}S_{V\text{-}CDT}$ from −1.3‰ to 3.9‰. The mean value for these grains is 1.5‰.

The analytical errors for the three types of pyrite were of similar magnitude and ranged from <1‰ to ~4‰, most commonly around 2‰. While these errors are clearly larger than those obtained by conventional gas source mass spectrometry, they are sufficiently small to trace most natural fractionations of sulphur isotopes by biological and non-biological means in the rock record.

Two areas of Type 1 pyrites are illustrated in Fig. 8. It is not possible to demonstrate the $^{34}S/^{32}S$ ratio as an image because the differences are only apparent on a grain-to-grain scale, and not on a pixel-to-pixel scale. The grains appear largely homogenous, with little evidence of zonation across a grain. The grain edges are not well defined due to small amounts of instrumental drift during the acquisition. Hence, the pixels at the edges of the grains were not selected for the isotope ratio measurements.

The mean of Type 1 pyrites (−2.1‰) is very similar to that of Type 2 (−2.9‰). This similarity in means between Type 1 and Type 2 pyrites demonstrates the amount of information that would have been lost had the pyrites not been analysed by NanoSIMS. For example, using laser ablation it would likely only have been possible to obtain one measurement from this entire area (using conventional powdering of the rock sample the spatial resolution would be many, many times worse); this measurement would have returned a value approximately equal to the mean of Type 1 and Type 2 pyrites (i.e. around −2.5‰). This value is not far removed from that for magmatic mantle-derived H_2S [+1 ± 1‰ (Ohmoto and Rye, 1979)]. Since the isotopic composition of non-biological magma-derived sulphides may range between 4–5‰ of this mantle value (Schneider, 1970), the most logical conclusion from bulk data would be that both Type 1 and Type 2 pyrites had formed non-biologically from hydrothermal or volcanogenic processes.

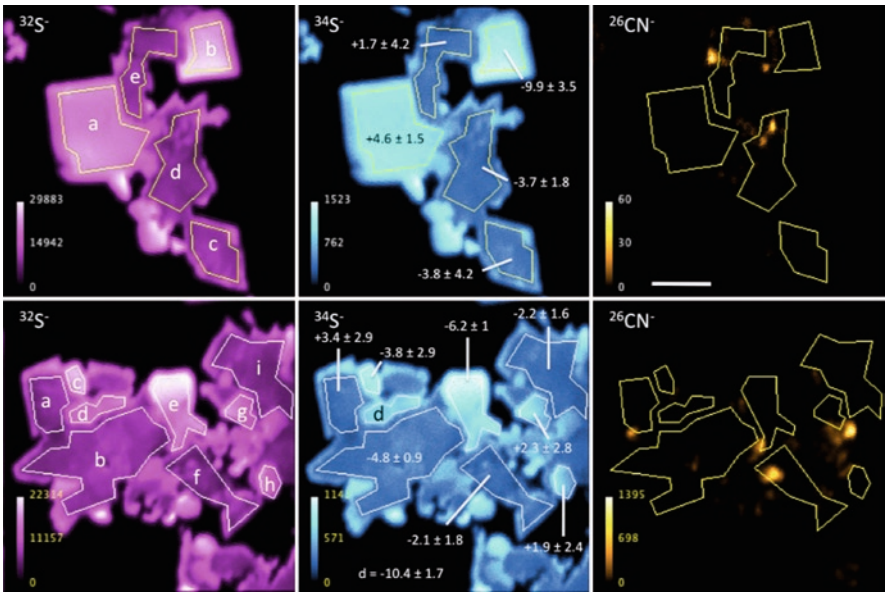

Figure 8. $\delta^{34}S$ measurement from Type 1 pyrite. NanoSIMS secondary ion images of $^{32}S^-$, $^{34}S^-$ and $^{26}CN^-$ associated with two areas of micron-sized (Type 1) pyrites within the Strelley Pool sandstone. *Black area* is background quartz. Cameca NanoSIMS Image processing software was used to isolate the pixels defining different grains (e.g. **a**–**e** on top row) in each image and then to ratio the $^{34}S^-$ counts to the $^{32}S^-$ counts for each grain. The $^{26}CN^-$ image shows organic matter associated with the pyrite. The mean $\delta^{34}S_{V\text{-}CDT}$ values (‰) for each grain with fully propagated errors are superimposed on the ^{34}S images. Scale bar is 2.5 μm. Colour scale is calibrated in counts per second.

In contrast, using NanoSIMS (Fig. 9), we see that the Type 1 pyrite exhibits a spread in $\delta^{34}S$ of 18‰ over less than 1 mm within the thin section, and a maximum ^{34}S depletion of about −15‰ from inferred early Archean seawater sulphate [$\delta^{34}S \sim +3$‰ (Strauss, 2003)]. This is of a similar magnitude to putative reports of biological sulphur processing in other early Archean sediments (Ohmoto et al., 1993; Shen et al., 2001; Shen and Buick, 2004; Philippot et al., 2007). This data does not give definitive evidence for biological participation in the formation of Type 1 pyrite, because non- biological processes such as reduction of sulphate by Fe^{2+}-bearing minerals (Ohmoto and Goldhaber, 1997) and thermochemical reduction by hydrocarbons (Machel, 2001) can impart fractionations of a similar magnitude. However, when combined with other evidence (e.g. close association of carbon and nitrogen with the Type 1 pyrites (Fig. 8), and field evidence for low temperature, syn-depositional to early diagenetic timing of formation of Type 1 pyrite), a biological formation mechanism appears the most plausible scenario. The modelling of this data to potentially determine the microbial metabolism and concentrations of sulphate in the Archean ocean is beyond the scope of this chapter; instead details can be found in Wacey et al. (2010b).

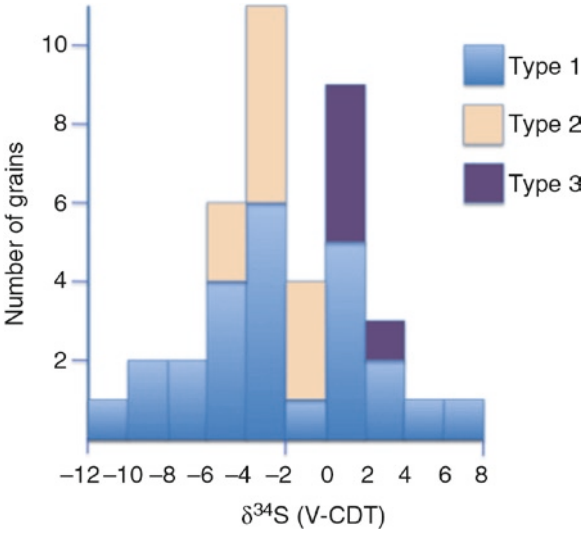

Figure 9. Stacked histogram of $\delta^{34}S$ data from three types of pyrite within the ~3.43 Ga Strelley Pool sandstone. Sixty-nine analyses on 25 individual grains were made for Type 1 pyrite, 44 analyses on ten grains for Type 2, and eight analyses on five grains for Type 3. This histogram reports the mean value for each individual grain.

The similarity in the mean values for Type 1 and Type 2 pyrites suggests that Type 2 may have formed from dissolution and recrystallisation of Type 1 during low-grade metamorphism. Type 3 pyrites exhibit $\delta^{34}S$ signatures (mean 1.5‰) within the range of values for igneous sulphides formed using H_2S derived from Archean magma (Ohmoto et al., 1993). These Type 3 detrital pyrites were likely eroded from a >3.43 Ga igneous body and then concentrated as placer deposits in the Strelley Pool sandstone.

2.3. CARBON ISOTOPE ANALYSIS

Carbon isotope measurements were made using an integration method, as the features were mostly large enough to completely fill the field of view. A slightly defocused Cs^+ primary beam was rastered over an area of 10×10 μm^2, made up of 64×64 pixels, and the counts per pixel were integrated over the total number of pixels per frame. To achieve the one million counts from the less abundant isotope, necessary for a precision of 1‰, 500 frames were measured for each analysis. Only counts from the central 44×44 pixels were recorded to eliminate the contribution from crater edge effects.

The mass spectrometer was tuned to allow the ^{13}C peak to be resolved from $^{12}C^1H$ on mass 13, while maintaining good counting statistics ($M/\Delta M = 3{,}000$, with 200k cps on ^{12}C). Counts for ^{12}C and ^{13}C were recorded simultaneously using EMs, and the ratio was calculated from the total counts recorded. The counts were corrected for instrumental effects, such as dead time and EM yield. Under these analytical conditions, detector ageing was negligible. QSA was considered negligible because the count rates for the standard and sample were very similar, so any QSA correction should not affect the relative $\delta^{13}C$ values between standard

and sample. This point still requires some clarification, however, as the extent of the QSA effect on carbon has yet to be accurately determined.

The carbon-rich material in our samples is largely kerogenous in nature, but its great age and metamorphism mean that it approaches a graphitic composition (although there is still some disorder seen in transmission electron microscopy and laser Raman spectra); thus, the NanoSIMS was calibrated using the graphite standard USGS-24, which has a $\delta^{13}C_{V\text{-}PDB}$ value of −16‰. $^{13}C/^{12}C$ raw ratios were converted to $\delta^{13}C$ values (in ‰) using the formula:

$$\delta^{13}C_{V\text{-}PDB}\% = [(^{13}C/^{12}C_{sample}) - (^{13}C/^{12}C_{standard}) \times 1{,}000$$

To reduce instrumental effects caused by the movement of the ion beam between sample holders, the grains of USGS-24, typically around 10 μm in diameter, were mounted directly within the sample thin-section close to the analysis area. The NanoSIMS was then tuned to give good spot-to-spot reproducibility on the standard before moving to the sample kerogen. Multiple analyses of several grains of USGS-24 gave $\delta^{13}C$ values with a 1σ external precision for the standard of 3‰.

2.3.1. Samples

Our NanoSIMS carbon isotope methodology was developed using kerogen from ambient inclusion trails (AITs) from a silicified sandstone at the base of the ~3.43 Ga Strelley Pool Formation (see Sect. 2.2.1 for geological setting). AITs are poorly understood microtubular structures that appear to be created by the migration of mineral crystals through a lithified or partly lithified substrate (Tyler and Barghoorn, 1963). One potential driving force behind this phenomenon is the decomposition of organic material attached to the mineral crystals (Knoll and Barghoorn, 1974). If such organic material could be shown to be biological, then AITs may be used as a biosignature for investigating early life on Earth. Wacey et al. (2008) have investigated AITs from the Strelley Pool Formation in some detail, this is summarised below.

AITs in the Strelley Pool sandstone are strictly substratum specific, confined to ~5% of rounded clasts, comprising well-preserved microcrystalline silica that contain small cubes of pyrite (Type 4 pyrite above). The microtubes are 1–15 μm in diameter, up to 300 μm in length and can be either hollow or filled with silica, ferrous phosphate, aluminium phosphate or jarosite (likely a younger contaminant). They exhibit a range of morphologies from straight, to curved, twisted or even helical, and are occasionally branched. Their diameter appears to remain constant along their length, and they commonly cluster around clots of organic matter. These have been interpreted as AIT for the following reasons (Wacey et al., 2008): they only occur in clasts rich in pyrite (or pseudomorphs after pyrite) and commonly also rich in organic matter; some still contain propelled terminal pyrite crystals (Fig. 10a); many microtubes originate from the centre of the silica grains and can move both inwards and outwards through the grain. In contrast, endolithic borings would only penetrate inwards from the edge of a grain; many of the microtubes have polygonal cross sections, consistent with the geometry of

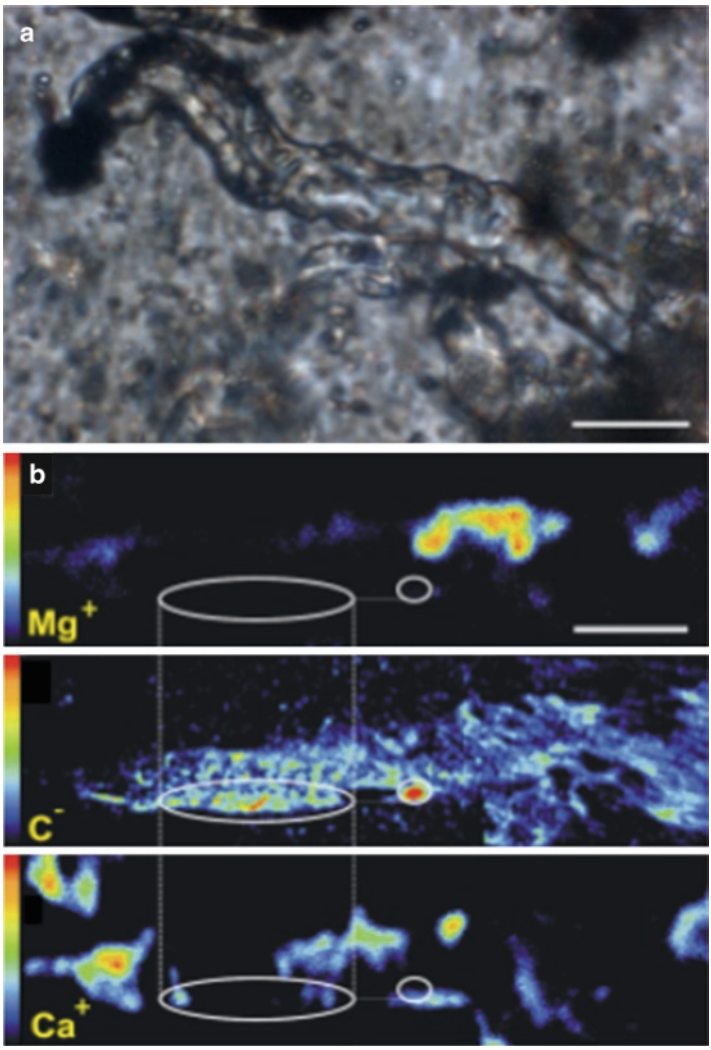

Figure 10. An ambient inclusion trail (AIT) from the ~3.43 Ga Strelley Pool sandstone. (**a**) Thin section photomicrograph showing an AIT with terminal pyrite crystal that has been propelled from the bottom right to the top left of the image. Note *dark areas* of organic material within the tubular structure; (**b**) NanoSIMS ion images of magnesium, carbon and calcium from an adjacent AIT, showing that carbon distribution is not correlated with either calcium or magnesium within the AIT. This indicates that the carbon is present in organic material and not a mineral phase such as carbonate. Oval areas indicate identical areas on each image. Scale bars are 10 μm. Part (**b**) is taken from Wacey et al. (2008).

a mineral grain, but inconsistent with microfossils or microbial borings. Our $\delta^{13}C$ measurements were made on carbon found within these AITs, mostly occurring as linings along tube edges.

A slightly modified version of our NanoSIMS carbon isotope methodology has also been used for solidified oil (pyrobitumen) and kerogen in ~2.63 Ga shales from the Jeerinah Formation, Pilbara Craton, Western Australia (see Rasmussen et al., 2008 for details).

2.3.2. Carbon Isotope Results

Using NanoSIMS, Wacey et al. (2008) found significant enrichments in carbon and nitrogen in AIT from the centre of microcrystalline silica grains in the Strelley Pool Formation. These enrichments corresponded to silica and oxygen depletion in the host grain and were often greatest in a narrow band at the outer edge of the AIT. Ca and Mg were present in some AITs but they did not correlate with carbon (Fig. 10b) indicating that the carbon was organic, not merely bound within a carbonate phase. Other potentially bio-limiting elements [e.g. P, S, K, Co, Fe, Ni, Zn (Frausto Da Silva and Williams, 2001)] were also correlated with carbon or concentrated in some way within the AIT infillings (Wacey et al., 2008).

NanoSIMS carbon isotope analysis was performed directly on the carbon rich interior of two AIT structures (AIT 1 and AIT 2). Five analysis points, each comprising 500 measurements, from AIT 1 resulted in a mean $\delta^{13}C_{V\text{-}PDB}$ value of −27.6‰; the errors for each analysis point were ~3.0‰. Four analysis points, again each comprising 500 measurements, from AIT 2 resulted in a mean $\delta^{13}C_{V\text{-}PDB}$ value of −24.0‰, and errors of 3.1–3.8‰. The errors on these analyses are around an order of magnitude higher than those obtainable by conventional gas-source mass spectrometry (e.g. Van Zuilen et al., 2002); clearly, NanoSIMS is not the technique to use in cases where very high precision is needed. However, there are many situations where spatial resolution is more important than high precision, and errors of ~3‰ do not compromise the interpretation of the data. This is often the case in the field of Precambrian palaeobiology where biological fractionations are relatively large [20–40‰ in favour of ^{12}C for enzymatic carboxylation reactions (Schidlowski, 1988)] but the microbes responsible are very small. In the case highlighted here, NanoSIMS is the only technique capable of measuring isotopes from the small amounts of carbon associated with these AIT structures, and gives data that is consistent with the biological C3 "Calvin cycle" carbon fixation pathway. Other carbon fixation pathways (e.g. C4 dicarboxylic acid or reductive acetyl coenzyme A pathways) do not fractionate carbon isotopes to the extent of the C3 Calvin Cycle (Schidlowski, 1988), but such biological signatures should still be resolvable using NanoSIMS.

3. Summary

NanoSIMS facilitates the in situ elemental and isotopic analysis of very small objects and the correlation of this data with morphological features observed in petrographic thin section, and with data from other techniques such as laser

Raman or electron microscopy. Applications of NanoSIMS are widespread through the geological and biological sciences; here, we have demonstrated its applicability for improving our understanding of chemical signals typical of life in both modern and ancient environments. The spatial resolution of the NanoSIMS allows detection and mapping of elements and isotopes within individual laminations of stromatolites, biominerals, trace fossils and microfossils. Quantitative isotope data can be obtained with 1–3‰ precision on objects as small as ~2 μm.

4. Acknowledgements

Our thanks go to Owen Green and Martin Brasier for provision of stromatolite samples, and to Adrian Boyce for laser ablation sulphur isotope analyses. DW is supported by a UPRF from The University of Western Australia. Both authors acknowledge the facilities, scientific and technical assistance of the Australian Microscopy and Microanalysis Research Facility at the Centre for Microscopy, Characterisation and Analysis, The University of Western Australia, a facility funded by The University, State and Commonwealth Governments. The authors thank P. Hoppe and an anonymous reviewer for comments that improved the quality of this chapter, and V. Tewari and J. Seckbach for the invitation to contribute to this book.

5. References

Allen, M.A., Goh, F., Burns, B.P. and Neilan, B.A. (2009) Bacterial, archaeal and eukaryotic diversity of smooth and pustular microbial mat communities in the hypersaline lagoon of Shark Bay. Geobiology **7**: 82–96.

Allwood, A.C., Walter, M.R., Kamber, B.S., Marshall, C.P. and Burch, I.W. (2006) Stromatolite reef from the Early Archaean era of Australia. Nature 441: 714–718.

Baumgartner, L.K., Reid, R.P., Dupraz, C., Decho, A.W., Buckley, D.H., Spear, J.R., Przekop, K.M. and Visscher, P.T. (2006) Sulfate reducing bacteria in microbial mats: changing paradigms, new discoveries. Sediment. Geol. **185**: 131–145.

Brasier, M., McLoughlin, N., Green, O. and Wacey, D. (2006) A fresh look at the fossil evidence for early Archaean cellular life. Philos. Trans. R. Soc. B **361**: 887–902.

Brown, R.G. (1983) Sea level history over the past 15,000 years along the Western Australian coastline, In: D. Hopley (ed.) *Australian Sea Levels in the Last 15,000 Years: A Review.* Department of Geography, James Cook University of North Queensland, Occasional Paper No. 3, pp. 28–36.

Buick, R. (1992) The antiquity of oxygenic photosynthesis – evidence from stromatolites in sulfate-deficient Archean lakes. Science **255**: 74–77.

Buick, R., Thornett, J.R., McNaughton, N.J., Barley, M.E. and Savage, M. (1995) Record of emergent continental crust ~3.5 billion years ago in the Pilbara craton of Australia. Nature **375**: 574–577.

Burns, B.P., Goh, F., Allen, M. and Neilan, B.A. (2004) Microbial diversity of extant stromatolites in the hypersaline marine environment of Shark Bay, Australia. Environ. Microbiol. **6**: 1096–1101.

Frausto Da Silva, J.J.R. and Williams, R.J.P. (2001) *The Biological Chemistry of the Elements: The Inorganic Chemistry of Life*, 2nd edn. Oxford University Press, Oxford.

Graham, C.M. and Valley, J.W. (1992) Sulfur analyses of pyrite. Chem. Geol. **101**: 169–172.
Grey, K., Moore, L.S., Burne, R.V., Pierson, B.K. and Bauld, J. (1990) Lake Thetis, Western Australia: an example of saline lake sedimentation dominated by benthic microbial processes. Aust. J. Mar. Freshwater Res. **41**: 275–300.
Grotzinger, J.P. and Knoll, A.H. (1999) Stromatolites in Precambrian carbonates: evolutionary mileposts or environmental dipsticks? Ann. Rev. Earth Planet. Sci. **27**: 313–358.
Grotzinger, J.P. and Rothman, D.H. (1996) An abiotic model for stromatolite morphogenesis. Nature **383**: 423–425.
Hayatsu, R., Studier, M.H., Matsuoka, S. and Anders, E. (1972) Origin of organic matter in early solar system – VI. Catalytic synthesis of nitriles, nitrogen bases and porphyrin-like pigments. Geochim. Cosmochim. Acta **36**: 555–571.
Hickman, A.H. (2008) Regional review of the 3426–3350 Ma Strelley Pool Formation, Pilbara Craton, Western Australia. Geol. Surv. West. Aust. Rec. **2008**(15): 27p.
Hillion, F., Daigne, F., Girard, F. and Slodzian, G. (1994) A new high performance instrument: the CAMECA NanoSIMS 50, In: A. Benninghoven, Y. Nihei, R. Shimizu and H.W. Werner (eds.) Secondary Ion Mass Spectrometry: SIMS IX. Wiley, New York, pp. 254–256.
Hillion, F., Kilburn, M.R., Hoppe, P., Messenger, S. and Weber, P.K. (2008) The effect of QSA on S, C, O and Si isotopic ratio measurements. Geochim. Cosmochim. Acta 72: A377.
Hofmann, H.J., Grey, K., Hickman, A.H. and Thorpe, R.I. (1999) Origin of 3.45 Ga Coniform Stromatolites in the Warrawoona Group, Western Australia. Bull. Geol. Soc. Am. **111**: 1256–1262.
Knoll, A.H. and Barghoorn, E.S. (1974) Ambient pyrite in Precambrian chert: new evidence and a theory. Proc. Nat. Acad. Sci. U.S.A. **71**: 2329–2331.
Kung, C., Hayatsu, R., Studier, M.H. and Clayton, R.N. (1979) Nitrogen isotope fractionation in the Fischer-Tropsch synthesis and in the Miller-Urey reaction. Earth Plan. Sci. Lett. **46**: 141–146.
Lepot, K., Benzerara, K., Brown Jr, G.E. and Philippot, P. (2008) Microbially influenced formation of 2,724-million-year-old stromatolites. Nat. Geosci. **1**: 118–121.
Logan, B.W., Hoffman, P. and Gebelein, C.D. (1974) Algal mats, cryptalgal fabrics, and structures, Hamelin Pool, Western Australia. Am. Assoc. Pet. Geol. Mem. **22**: 140–194.
Lowe, D.R. (1980) Stromatolites 3,400-Myr old from the Archean of Western Australia. Nature **284**: 441–443.
Lowe, D.R. (1983) Restricted shallow-water sedimentation of early Archaean stromatolitic and evaporitic strata of the Strelley Pool chert, Pilbara block, Western Australia. Precambrian Res. **19**: 239–283.
Lowe, D.R. (1994) Abiological origin of described stromatolites older than 3.2 Ga. Geology **22**: 387–390.
Machel, H.G. (2001) Bacterial and thermochemical sulfate reduction in diagenetic settings – old and new insights. Sediment. Geol. **140**: 143–175.
McCollum, T.M. and Seewald, J.S. (2006) Carbon isotope composition of organic compounds produced by abiotic synthesis under hydrothermal conditions. Earth Planet. Sci. Lett. **243**: 74–84.
McLoughlin, N., Wilson, L. and Brasier, M.D. (2008) Growth of synthetic stromatolites and wrinkle structures in the absence of microbes – implications for the early fossil record. Geobiology 6: 95–105.
Oehler, D.Z., Robert, F., Mostefaoui, S., Meibom, A., Selo, M. and McKay, D.S. (2006) Chemical mapping of Proterozoic organic matter at submicron spatial resolution. Astrobiology **6**: 838–850.
Ohmoto, H. and Goldhaber, M.B. (1997) Sulphur and carbon isotopes, In: H.L. Barnes (ed.) *Geochemistry of Hydrothermal Ore Deposits*, 3rd edn. Wiley, New York, pp. 517–611.
Ohmoto, H. and Rye, R.O. (1979) Isotopes of sulphur and carbon, In: H.L. Barnes (ed.) *Geochemistry of Hydrothermal Ore Deposits*, 2nd edn. Wiley, New York, pp. 509–567
Ohmoto, H., Kakegawa, T. and Lowe, D.R. (1993) 3.4-billion-year-old pyrites from Barberton, South Africa: sulfur isotope evidence. Science **262**: 555–557.
Papineau, D., Walker, J.J., Mojzsis, S.J. and Pace, N.R. (2005) Composition and structure of microbial communities from stromatolites of Hamelin Pool in Shark Bay, Western Australia. Appl. Environ. Microbiol. **71**: 4822–4832.

Philippot, P., Van Zuilen, M., Lepot, K., Thomazo, C., Farquhar, J. and Van Kranendonk, M.J. (2007) Early Archean microorganisms preferred elemental sulfur, not sulfate. Science **317**: 1534–1537.

Playford, P.E. (1990) Geology of the Shark Bay area, Western Australia, In: P.F. Berry, S.D. Bradshaw and B.R. Wlison (eds.) *Research in Shark Bay*. Report of the France-Australe Bicentenary Expedition Committee, Western Australian Museum, pp. 13–33.

Rasmussen, B., Fletcher, I.R., Brocks, J.J. and Kilburn, M.R. (2008) Reassessing the first appearance of eukaryotes and cyanobacteria. Nature **455**: 1101–1104.

Reid, R.P., James, N.P., Macintyre, I.G., Dupraz, C.P. and Burne, R.V. (2003) Shark Bay stromatolites: microfabrics and reinterpretation of origins. Facies **49**: 299–324.

Riciputi, L.R., Paterson, B.A. and Ripperdan, R.L. (1998) Measurement of light stable isotope ratios by SIMS: matrix effects for oxygen, carbon, and sulfur isotopes in minerals. Int. J. Mass Spectrom. 178: 81–112.

Robert, F., Selo, M., Hillion, F. and Skrzypczak, A. (2005) NanoSIMS images of Precambrian fossil cells. LPSC XXXVI, abstract 1314.

Runnegar, B., Dollase, W.A., Ketcham, R.A., Colbert, M. and Carlson, W.D. (2001) Early Archaean sulphates from Western Australia first formed as hydrothermal barites not gypsum evaporites. Geol. Soc. Am. Abstr. Prog. **33**: A-404.

Sakurai, R., Ito, M., Ueno, Y., Kitajima, K. and Maruyama, S. (2005) Facies architecture and sequence-stratigraphic features of the Tumbiana Formation in the Pilbara Craton, northwestern Australia: implications for depositional environments of oxygenic stromatolites during the Late Archean. Precambrian Res. **138**: 255–273.

Schidlowski, M. (1988) A 3,800-million-year isotopic record of life from carbon in sedimentary rocks. Nature **333**: 313–318.

Schneider, A. (1970) The sulfur isotope composition of basaltic rocks. Contrib. Mineral. Petrol. **25**: 95–124.

Schopf, J.W. (2006) The first billion years: when did life emerge? Elements **2**: 229–233.

Semikhatov, M.A., Gebelein, C.D., Cloud, P., Awramik, S.M. and Benmore, W.C. (1979) Stromatolite morphogenesis: progress and problems. Can. J. Earth Sci. **16**: 992–1015.

Shen, Y. and Buick, R. (2004) The antiquity of microbial sulfate reduction. Earth Sci. Rev. **64**: 243–272.

Shen, Y. Buick, R. and Canfield, D.E. (2001) Isotopic evidence for microbial sulphate reduction in the early Archean era. Nature **410**: 77–81.

Slodzian, G., Chaintreau, M., Dennebouy, R. and Rousse, A. (2001) Precise in situ measurements of isotopic abundances with pulse counting of sputtered ions. Eur. Phys. J. Appl. Phys. **14**(3): 199–231.

Slodzian, G., Hillion, F., Stadermann, F.J. and Zinner, E. (2004) QSA influences on isotopic ratio measurements. Appl. Surf. Sci. **231–232**: 874–877.

Strauss, H. (2003) Sulphur isotopes and the early Archaean sulphur cycle. Precambrian Res. **126**: 349–361.

Tice, M.M. and Lowe, D.R. (2004) Photosynthetic microbial mats in the 3,416-Myr-old ocean. Nature **431**: 549–552.

Tyler, S.A. and Barghoorn, E.S. (1963) Ambient pyrite grains in Precambrian cherts. Am. J. Sci. **261**: 424–432.

Ueno, Y., Isozaki, Y., Yurimoto, H. and Maruyama, S. (2001) Carbon isotopic signatures of individual Archean microfossils (?) from Western Australia. Int. Geol. Rev. **43**: 196–212.

Van Zuilen, M.A., Lepland, A. and Arrhenius, G. (2002) Reassessing the evidence for the earliest traces of life. Nature **418**: 627–630.

Wacey, D. (2009) *Early Life on Earth: A Practical Guide*. Springer, Amsterdam, 285 p. ISBN 978-1-4020-9388-3.

Wacey, D., McLoughlin, N., Green, O.R., Stoakes, C.A. and Brasier, M.D. (2006) The ~3.4 billion-year-old Strelley Pool Sandstone: a new window into early life on Earth. Int. J. Astrobiol. **5**: 333–342.

Wacey, D., Kilburn, M.R., McLoughlin, N., Parnell, J., Stoakes, C.A., Grovenor, C.R.M. and Brasier, M.D. (2008) Use of NanoSIMS in the search for early life on Earth: ambient inclusion trails in a c. 3400 Ma sandstone. J. Geol. Soc. London **165**: 43–53.

Wacey, D., McLoughlin, N., Stoakes, C.A., Kilburn, M.R., Green, O.R. and Brasier, M.D. (2010a) The 3426–3350 Ma Strelley Pool Formation in the East Strelley greenstone belt – a field and petrographic guide. Geol. Surv. West. Aust. Rec. **2010**(10), 64p.

Wacey, D., McLoughlin, N., Whitehouse, M.J. and Kilburn, M.R. (2010b) Two coexisting sulfur metabolisms in a ca. 3400 Ma sandstone. Geology **38**: 1115–1118.

Walsh, M.M. and Lowe, D.L. (1999) Modes of accumulation of carbonaceous matter in the early Archean: a petrographic and geochemical study of the carbonaceous cherts of the Swaziland Supergroup, In: D.R. Lowe and G.R. Byerly (eds.) *Geologic Evolution of the Barberton Greenstone Belt, South Africa*. Geol. Soc. Am. Spec. Pap. 329. Boulder, Colorado, pp. 167–188.

Walter, M.R. (1972) *Stromatolites and the Biostratigraphy of the Australian Precambrian and Cambrian*. The Palaeontological Association, London.

Walter, M.R. (1976) Introduction, In: M.R. Walter (ed.) *Stromatolites.* Elsevier, Amsterdam, pp. 1–3.

Walter, M.R., Buick, R. and Dunlop, J.S.R. (1980) Stromatolites, 3,400–3,500 Myr old from the North Pole area, Western Australia. Nature **284**: 443–445.

Winterholler, B., Hoppe, P., Foley, S. and Andreae, M.O. (2008) Sulfur isotope ratio measurements of individual sulfate particles by NanoSIMS. Int. J. Mass Spectrom. **272**: 63–77.